Lithography-free broadband visible light absorber based on a mono-layer of gold nanoparticles

2014 J. Opt. 16 025002

(http://iopscience.iop.org/2040-8986/16/2/025002)

IOP Publishing Journal of Optics
J. Opt. **16** (2014) 025002 (9pp) doi:10.1088/2040-8978/16/2/025002

Lithography-free broadband visible light absorber based on a mono-layer of gold nanoparticles

M Yan, J Dai and M Qiu

Optics and Photonics, School of Information and Communication Technology, KTH-Royal Institute of Technology, Electrum 229, Kista SE-16440, Sweden

E-mail: miya@kth.se

Received 22 October 2013, revised 29 November 2013
Accepted for publication 6 December 2013
Published 15 January 2014

Abstract

We experimentally demonstrate a large area, optically opaque plasmonic absorber which can absorb 95% of visible light with an effective thickness of less than 150 nm. The absorber comprises, from top to bottom, a mono-layer of random gold nanoparticles, a dielectric spacer, and a bottom gold reflector. Reflectometry analyses show that its absorption is insensitive to the incidence's polarization or angle when the incident angle is less than 50°. At a larger incident angle, reflection increases and absorption spectra differ for two polarizations. Numerical simulations based on a 3D finite-element method suggest that the high absorbance is due to collective efforts of dipolar particle resonances, most often strongly coupled and forming chain resonances, as well as coupling of light to the surface plasmon polariton, *irrespective of the incidence's polarization*, through the top-layer particles. Similar high absorptivity is also demonstrated with silver or aluminum as the bottom reflector. These highly efficient visible light absorbers can be potential candidates for a range of passive and active photonic applications, including solar-energy harvesting as well as producing artificial colors on a large scale.

Keywords: plasmonics, absorber, metamaterial, optical absorption, metallic nanostructure
PACS numbers: 42.25.Bs, 81.05.Xj, 78.67.Pt, 73.20.Mf, 78.66.Sq

S Online supplementary data available from stacks.iop.org/JOpt/16/025002/mmedia

1. Introduction

The visual appearance of some glasses containing nanoparticles of certain noble metals, especially gold ruby glass, has long attracted academic interest and was critically analyzed by prominent scientists like Zsigmondy [1] as well as Garnett [2, 3]. Coloring of these materials is caused by strong spectrally selective absorption and scattering of light by colloidal nanoparticles, physically incurred most often by the dipolar resonances supported by the particles. This work revisits the classic subject with a slightly different geometric setting: we study strong light absorption and therefore coloring by a mono-layer of gold nanoparticles of random sizes, assisted by an optically thick metal reflector that is placed tens of nanometers away. A dielectric spacer is in place between the two metal layers. The total thickness of the three layers is just around 150 nm. Surprisingly, such a simple plasmonic nanostructure can absorb 95% of visible light (390–700 nm in wavelength) and a significant portion of near-infrared light.

The optical properties of a mono-layer of metal nanoparticles on a dielectric substrate have been extensively investigated during the last 50 years and even beyond [4–12]. Some of these experimental investigations happened well before the advent of nano-fabrication technologies. One popular fabrication method used is based on the fact that an ultrathin gold film, when heated to a temperature well below the melting temperature of gold, can break into minute particles with nanometric sizes. Agglomeration of gold atoms or clusters,

facilitated by the forces of crystallization and surface tension when the film undergoes softening, is generally accepted as the process behind the formation of nanoparticles [13]. People in the thin-film community sometimes refer to such a mono-layer of metal nanoparticles as a 'metal-island film'. Three-layer planar structures similar to what is under study in this work have also been mentioned in a number of research publications for the purpose of achieving light absorption [5, 14–19]. The majority of these works however deal with a periodic top layer, where the particles are patterned regularly with a lithographic technique. Such a regular structure usually results in one or several relatively narrow absorption band(s). Attempts to broaden the absorption band were also reported, but also with a lithographic technique [20, 21].

In order to achieve absorption bands at visible frequencies, one should pattern the top-layer gold particles with sizes significantly less than 100 nm. Such a fine structure can be inscribed by the generic electron-beam lithography, which however limits the finished sample size to be less than 1 mm by today's technological standard. There exist several reports in which the top-layer gold nanoparticles are formed with a technique involving a chemical synthesis of particles plus a subsequent transfer of the particles on a pre-prepared substrate [22, 23]. This approach suffers from problems like particle aggregation or nonuniformity in particle distribution. A group also tried to use the magnetron-sputtering technique to deposit a gold–dielectric nano-composite layer onto a prepared substrate [24]. Though exhibiting slightly superior absorptivity, the samples obtained with this approach are more complex in structure and the absorption is quite difficult to comprehend, even numerically. A possibly viable method for fabricating a similar mono-layer of nanoparticles is the so-called colloidal lithography method [25]. As mentioned, this work borrows the technique of forming metallic-island films to fabricate gold nanoparticles. The particles fabricated have random sizes but with relatively uniform separations; therefore, they are free from aggregation. The average size of the particles can be controlled during film deposition and postprocessing. Experimentally such samples are prepared in a two-step process without using lithography. Our presentation will mainly focus on a sample with the highest absorptivity at the visible spectrum prepared with a gold bottom reflector. The high absorptivity remains almost the same when the incident angle is less than 50°, and persists even at a higher incident angle. Absorption efficiencies are found to be similar with a silver or an aluminum bottom reflector, instead of a gold reflector. 3D finite-element simulation reveals that key contributing factors for absorption include dipolar resonances of the gold nanoparticles (most often strongly coupled), as well as coupling of incident light to the surface plasmon polariton (SPP) guided by the reflector–spacer interface. The efficient light absorption capability of such a metamaterial surface (metasurface) despite its thinness at optical frequencies implies that they can be deployed for solar-energy harvesting and the design of optical components for achieving a certain visual appearance. The strong near fields due to plasmonic resonances sustained by the top-layer gold particles also promise applications in e.g. nonlinear optics.

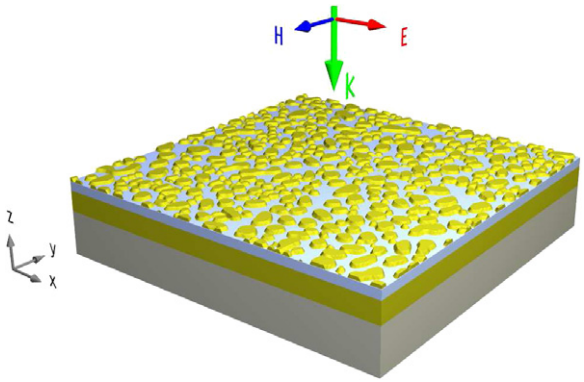

Figure 1. 3D schematic diagram of the fabricated absorber sample.

2. Sample geometry and preparation

The sample is fabricated in a two-stage process. First, three layers, namely an 80 nm-thick gold reflector, a 55 nm-thick alumina layer, and a 5-nm gold, are deposited sequentially on a dummy substrate (Si in our case) at a pressure of 5×10^{-7} mbar using an electron-beam-evaporation deposition machine (PROVAC PAK 600); the respective deposition rates are all nominally 1 Å s^{-1}. It should be noted that the actual deposition rate starts from a low value to the nominal value. The average deposition rate for the top gold layer is 0.5 Å s^{-1}. The sample is then put into an oven (Nabertherm Model L3) and annealed at a temperature of several hundreds of degrees simply in an air environment. The annealing step is to promote softening and agglomeration of the gold material in the top layer, resulting in well-separated gold nano-islands. The final sample after annealing has a geometry as illustrated in figure 1. The top layer has well-separated gold particles with lateral sizes less than 100 nm owing to the above-described annealing process. Besides using gold as the bottom reflector, we also fabricated samples with silver or aluminum as the bottom reflector. The three types of samples will be referred to as Au, Ag and Al samples, despite the fact that they all have gold particles on top.

The annealing process is governed by two important parameters, i.e. the maximum temperature and the annealing duration. Although in the following text we will just use a fixed temperature to refer to a particular annealing process, the actual temperature has a rather gentle temporal profile due to slow ramp-up and cooling processes. See supplementary data (available at stacks.iop.org/JOpt/16/025002/mmedia) for the exact temperature profiles. All annealings last for about one hour. The gold sample with the highest absorptivity is annealed under 350 °C. It is critical to know that the annealing process does not affect the integrity of the bottom-layer gold reflector nor that of the spacer layer, especially when the annealing temperature is set not higher than 350 °C. This is primarily due to the fact that the spacer material (alumina) has a very high melting temperature. The annealing temperature highly influences the geometries of the resulting top-layer particles. In figures 2(a)–(d) the top views of the sample as deposited and those annealed at various temperatures are shown. The images are obtained using a high-resolution scanning-electron

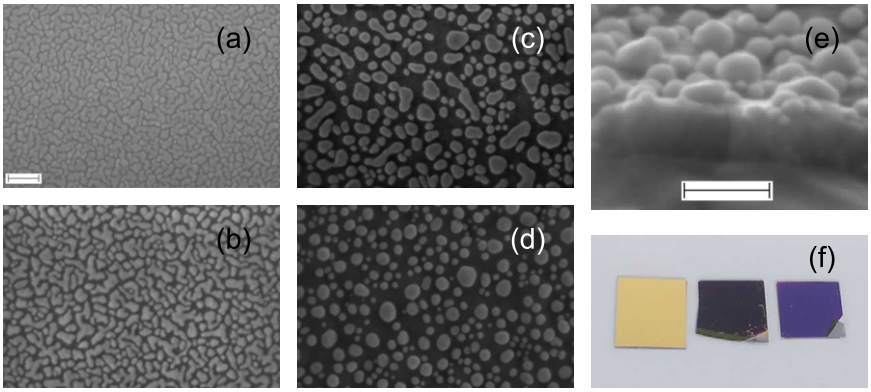

Figure 2. Top-view SEM images of the samples as deposited (a), annealed at 200 °C (b), annealed at 350 °C (c), and annealed at 500 °C (d). (a)–(d) Share the same scale bar (100 nm) as indicated in (a). (e) Side view of an Al sample annealed at 500 °C. Scale bar represents again 100 nm. (f) Photograph of (from left to right) a sample coated with 80 nm gold, sample in (c), and sample in (e) in a daylight-lit room environment. The samples, with side lengths around 1 cm, are placed on a common printing paper.

microscope (SEM). Note that even the as-deposited 5 nm-thick gold film is not continuous. From the SEM images, we see that the top-layer gold film becomes more discontinuous when the temperature increases. A higher annealing temperature makes the particles appear more circular as viewed from the top.

Note that one can obtain similar gold or silver samples (i.e. with a mono-layer of nanoparticles on top) without resorting to a post-thermal annealing procedure, if one can control the substrate temperature during deposition. For example, a substrate temperature over 200 °C was used in [26] to facilitate particle formation during deposition. [24] also hints that a mono-layer of gold particles can also be deposited directly with the magnetron-sputtering process. Nevertheless, a post-thermal annealing step can be utilized to further tune samples' absorption properties towards certain applications.

In figure 2(f), we show a camera view of the sample (in the middle) with its nanostructure given in figure 2(c); to its left we see the appearance of gold (film); to its right we see the appearance of an Al sample which shares the same particle layer as figure 2(d). From the photograph, one can easily tell that the middle sample exhibits a very high level of absorption across the visible spectral range. In fact, this particular sample has the highest absorption strength in the visible region among all samples made with the same preparation technique with different spacer thicknesses (from 10 to 100 nm). For this reason we pay special attention to this sample (i.e. with a 55 nm spacer thickness) in this report. In general, the samples fabricated exhibit a broad absorption band with a linewidth of a few hundred nanometers in wavelength. The band position red-shifts as the spacer thickness increases. At a spacer thickness of 55 nm, the absorption band overlaps well with the visible spectral region. Note that previous reports on seemingly similar absorber structure use a much thinner spacer (e.g. 10 nm Al_2O_3 in [18], 20 nm SiO_2 in [27], and 5–10 nm polymer in [22]). Samples in those works rely on the so-called magnetic-dipole resonance as explained in [18, 22, 27, 28], whereas the current absorber relies dominantly on a set of different light absorption mechanisms, as will be clarified in section 4. This difference is fundamentally caused by the fact that particle-to-particle separations in the top layer of our structure are in general smaller than particle-to-reflector separation.

From a high-resolution SEM image of the sample, we made a histogram on the particle sizes based on 1574 particles distributed over a sample area of $2 \times 2\ \mu m^2$. Here the size of a particle is defined as the diameter of a circular disk-shaped particle with an equivalent top area. The distribution is shown in figure 3. The mean size of the particles is found to be 32 nm, with a standard size deviation of 15 nm. The analysis also tells that the filling factor of the gold particles over the sample plane is $f = 41\%$, which suggests that the average thickness of the particle layer is about $5\ \text{nm}/f = 12.2$ nm. Note that the whole analysis is based on a top-view SEM image; it neglects potential fluctuations in particle heights. The heights of particles are not uniform, which is especially true when the sample is annealed at a high temperature, as can be seen from figure 2(e).

3. Optical characterization

The reflectance (R) spectra of three samples, which were annealed at different temperatures, are measured using an integrating sphere. The incident light is unpolarized with an incident angle of 8°. Both specular and diffusive (if exists) reflectances are included in such a reflection measurement. Owing to the thick gold reflector, light transmittance through the samples is negligible. The absorbance by the samples is therefore calculated as $1 - R$. The measurement results are shown in figure 4. From the figure it is seen that even the original sample before annealing exhibits a certain level of absorption in the visible wavelength region. Still, reflectances of about 12–15% are found for wavelengths between 600 nm (orange) to 700 nm (red). When the sample is annealed, its absorption strength increases, especially at the above-mentioned long-end of the visible wavelength range. The sample annealed at 350 °C exhibits a highest absorbance of 98.3%; and in average it absorbs 95.4% of visible light. This explains why the sample appears black. For comparison purposes, the absorption spectrum of the ideal gold–alumina–gold structure,

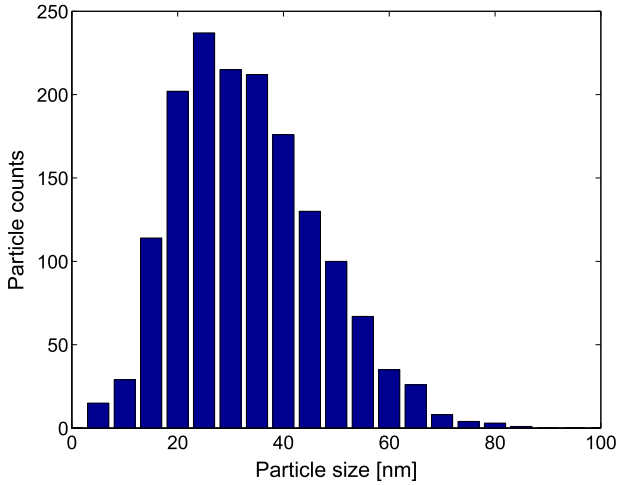

Figure 3. Distribution of the particle sizes of the fabricated sample, evaluated based on 1574 particles over an area of approximately $2 \times 2\ \mu m^2$.

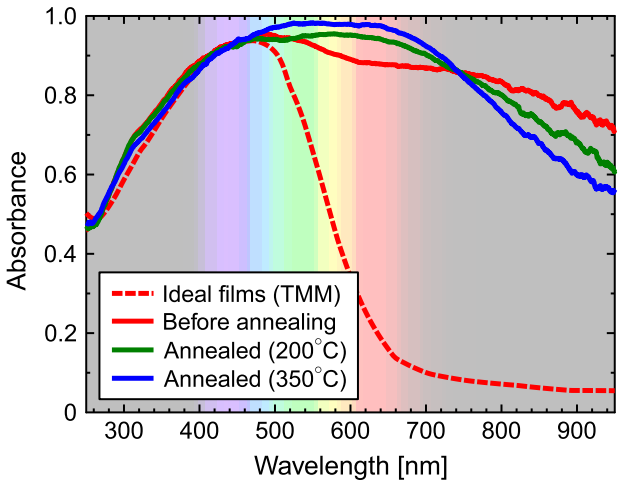

Figure 4. Effect of annealing temperature on the absorption spectrum. The color-coded visible spectrum is superimposed in the background of the plot.

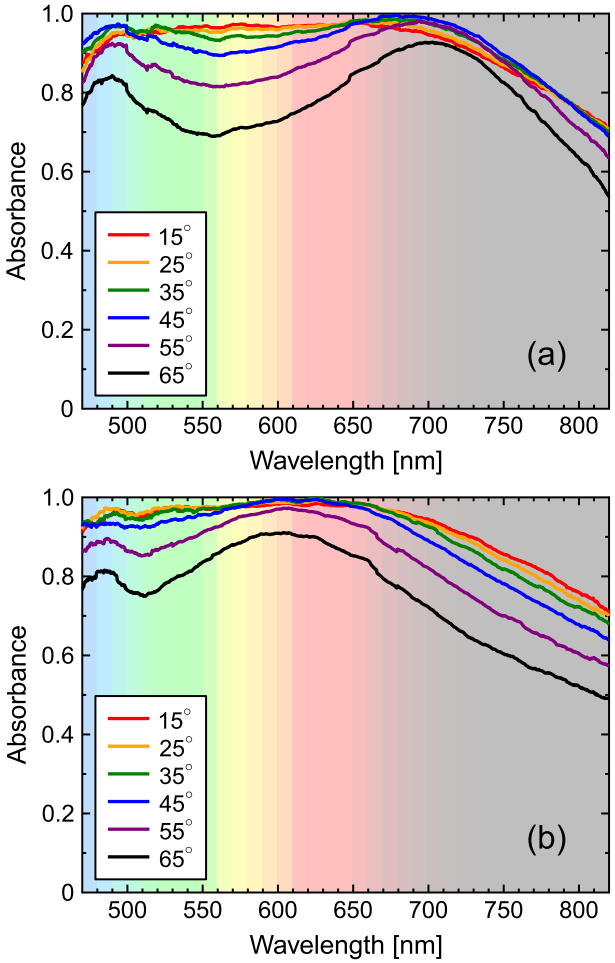

Figure 5. Angle-dependent absorption spectra for TE (a) and TM (b) incident polarizations. The curves appear slightly noisier than those in figure 4 because of the weaker light intensity owing to the additional polarizer and lenses used in the measurement setup. Nevertheless, we find that the measurement error in the spectral range of 550–820 nm is within 1.5%, and on the short wavelength side within 3%.

with layer thicknesses of 5, 55, and 80 nm from top to bottom, is also shown in the figure. The curve is calculated with an analytical transfer-matrix method (TMM) [29]. An average of the transverse-electric (TE) and transverse-magnetic (TM) absorption spectra is used for obtaining the current unpolarized absorbance curve. The optical constants of gold are taken from [30] and that for alumina from [31]. By comparing the theoretical curve with that of the sample before annealing, one immediately knows that the as-deposited 5-nm gold film (as shown in figure 2(a)) deviates greatly from an idealized flat film in its optical responses, especially at long wavelengths. The strong deviation in effective permittivity for gold-island films from bulk gold's permittivity is widely known [13]. This fact has been exploited for fabricating colored samples with a single layer of gold-island film [26].

To further probe the properties of the sample annealed at 350 °C, we measured the angle-dependent absorbance spectra, independently for two incident polarizations; the results are presented in figure 5. The spectra are obtained with an in-house setup, in which the specularly reflected light by the sample is collected by an integrating sphere, which is in turn optically connected to a spectrometer. In general for both incident polarizations, the reflection by the sample increases with the incident angle; the increase is however not significant for incident angles less than 50°. For TE incidence (figure 5(a)), the curves exhibit two distinct peaks. The peak on the left stays at around 480 nm wavelength irrespective of the incidence angle. The peak on the longer wavelength side, which is not obvious at a small incident angle, becomes more prominent and at the same time exhibits a red-shift when the incident angle increases. The TM incidence also induces two absorbance peaks, one at, again, 480 nm and the other at a longer wavelength, which exhibits a blue-shift when the incident angle increases.

The relatively stable absorbance peak around 480 nm, for both polarization cases, is considered to be mainly due to the interband transition of gold both in the bottom reflector and in the top gold nanoparticles. Our investigation also suggests that the strength of this absorption peak is affected by the

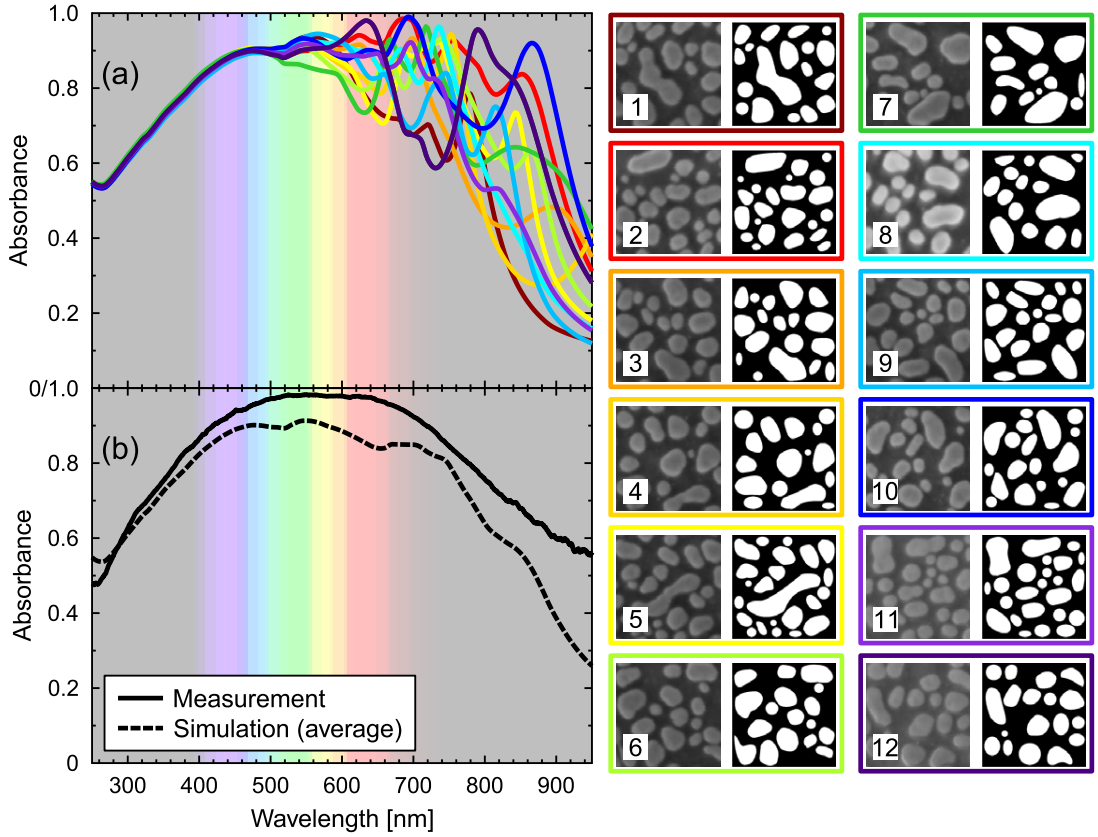

Figure 6. (a) Calculated normal-incident absorption spectra based on 12 sample regions taken from high-resolution SEM images. The corresponding SEM images used for calculation are shown in the insets. The sample regions are numbered as 1–12. Colors of the image frames correspond to colors of the absorption spectra curves. (b) Experimentally measured absorption spectrum and the averaged absorption curve based on the 12 simulations in (a).

spacer thickness. The absorption peaks at longer wavelengths for two incident cases are fundamentally related to excitation of dipolar resonances in the particles, as will be explained with the assistance of numerical simulations.

We shall remark that the sample, though containing discrete particles on top, can be considered flat when probed by visible light. The argument can be validated by comparing the absorption spectra of the same sample obtained by a direct integrating-sphere measuring technique and that by the reflectometry setup measuring only the specular reflection. More exactly, the blue curve in figure 4 has excellent agreement with the red curve in figure 5(a) or (b).

4. Simulation

To better reveal the high-absorption capabilities of the absorber, we have carried out full-vector 3D simulations using a finite-element method (FEM), with the help of the commercial package COMSOL multiphysics. The random structure is numerically un-swallowable without taking a finite sampling of the structure. Our numerical simulation was carried out as follows. First, a 200×200 nm^2 region was cropped out of a high-resolution top-view SEM image of the sample, as shown in the inset of figure 6. The boundaries of the particles were then traced out. The binary images were then imported into COMSOL and translated to geometries. The heights of the particles were assumed to be uniform, at 12 nm. Geometry definition was completed by adding spacer, reflector and air layers. This block, with a lateral extent of 200×200 nm^2, was then treated as a unit cell, which repeats over the particle plane (xy plane). Perfectly matched layers were placed both above and below the layered structure to absorb any transmitted or reflected waves. A similar way of simulating optical properties of metallic films with random features was also reported in [32]. The simulation was then repeated for 11 other regions on the sample with the same procedure. Finally an average of the 12 simulated absorption spectra was taken to obtain our final result. The material parameter for gold is again from [30] and that of alumina is from [31].

The results of our simulations are summarized in figure 6. In figure 6(a), we show the 12 simulated absorption spectra. The curves correspond to the samples (shown as insets on the right) by their color indications. The average of the 12 curves is shown in figure 6(b) as the dashed curve. By comparing the curve against the measured one (solid curve), one finds a reasonable agreement. Possible improvements in agreement can be made by introducing finite-size correction to gold's permittivity. Nonuniformity in particle heights can also be incorporated for more realistic simulations. However, our 'first-order' approximation of the problem can nevertheless capture the basic physics for explaining the high absorptivity.

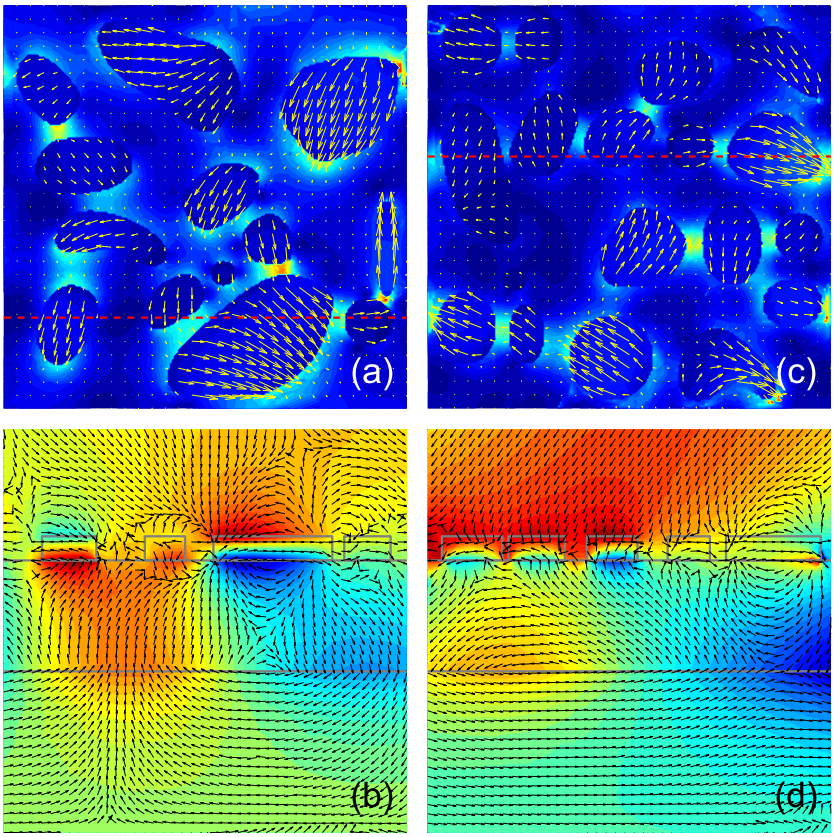

Figure 7. Field distributions for two scenarios, both with xz incidence plane. (a), (b) Sample No. 7; polarization: TE; incidence angle: 65°; wavelength: 720 nm. (c), (d) Sample No. 12; polarization: TM; incidence angle: 65°; wavelength: 650 nm. (a) Cut plane: xy plane through the center of the particles; arrows: in-plane displacement field ($\mathbf{D}_{xy}$); color map: norm of electric field. (b) Cut plane: xz plane through the red dashed line in (a); arrows: in-plane displacement field ($\mathbf{D}_{xz}$); color map: H_y. (c) Same cut plane and fields as in (a); (d) same field components as in (b) with the cutplane (xz) through the dashed line in (c). The domain sizes are the same for all plots, at 200×200 nm^2.

To identify the physical origins behind the sample's strong absorptivity, we look into electromagnetic field distributions in two representative scenarios. Figures 7(a) and (b) show the field distributions for sample region No. 7 when the incident light (with wavelength 720 nm) is TE polarized and has an incident angle of 65°. The incident plane is the xz plane; therefore, the incident light has field components E_y, H_x, and H_z. Panel (a) shows an xy cut plane through the center of the nanoparticles, with arrows indicating the $\mathbf{D}_{xy}$ field and a color map indicating the norm of the total electric field. Panel (b) shows an xz cut plane, with arrows indicating the $\mathbf{D}_{xz}$ and a color map indicating the H_y field. From figure 7(a), one sees that electrical dipoles within the gold nanoparticles are obviously excited; field strengths inside the particles are much larger than in the surrounding medium. At very small air gaps between two particles (with gap sizes at a few nanometers), strong gap plasmon resonances also appear. Individual dipole resonance for a gold particle with size close to 30 nm exhibits a bandwidth at full-width-at-half-maximum (FWHM) of ∼50 nm, as examined from its transmission spectrum [7]. Around the same bandwidth is found for resonances of dimers or bowtie antennas with a gap size of a few nanometers [23, 33]. Given our relatively random structure, numerous dipole and gap plasmon resonances occurring around dissimilar frequencies should collectively result in an ultra-broadband resonance. The overall absorption bandwidth of the broadband resonance should correlate to particle-size and gap-size statistics. The dipole resonances are most often strongly coupled, forming chain- or network-like resonators, which is also evident in figures 7(a) and (c). This strong coupling in particle resonances will cause further smearing-out of individual resonance peaks and will at the same time induce a red-shift of the overall absorption band. Red-shifting of particle resonances due to aggregation of gold particles in liquid has previously been reported in [34].

Not only do the gold nanoparticles' own dipolar and dipolar-based resonances cause light absorption over a broadband wavelength range, but also the random nanoparticles serve as mediators which couple the incident light to SPPs guided by the bottom reflector–spacer interface. A previous theoretical investigation on coupling between localized particle plasmons and SPPs was reported in [16]. In our structure, the coupling of incident light to the SPP can be incurred via two mechanisms. First, the top-layer particles serve as a random supergrating (a superposition of gratings), which couples especially the TM-incident light to SPPs guided by the reflector–spacer interface. The second mechanism is not as straightforward. At a distance very close to the gold nanoparticles, the dipolar electromagnetic fields are highly inhomogeneous. Such a near field of a dipole

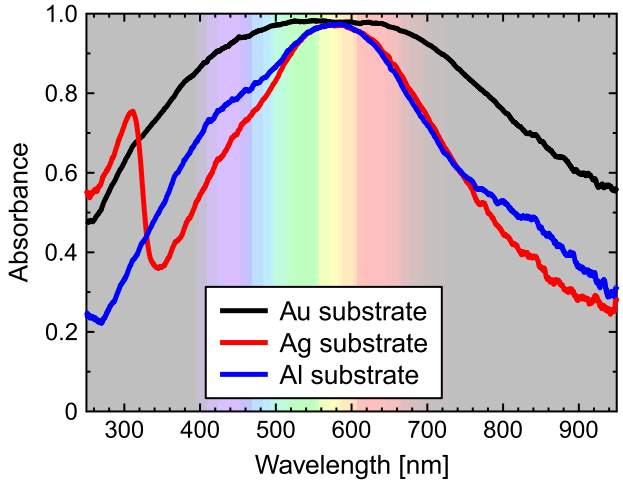

Figure 8. Absorption spectra for samples fabricated with various bottom reflectors, annealed at 350 °C. Incident light is unpolarized, and has an incident angle of 8°.

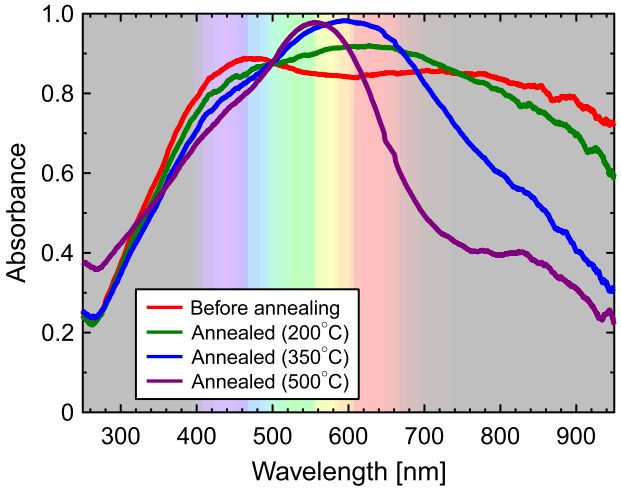

Figure 9. Absorption spectra for samples fabricated with an aluminum bottom reflector, annealed at various temperatures. Incident light is unpolarized, and has an incident angle of 8°.

radiation comprises a wide spectrum of wavevectors (if one spatially Fourier transforms the near field); light with a certain wavevector component can match that of a SPP guided by the reflector–spacer interface. Note that the second light coupling mechanism happens regardless of the incidence's polarization. Geometrically, the existence of random nanoparticles has destroyed the translational symmetry of the whole structure. Hence, there is no pure TE or TM electromagnetic system any more, especially at nanometers away from the particle layer. As shown by figures 7(b) and (d), SPPs are indeed excited at the reflector–spacer interface for both polarization cases. Owing to material loss of gold, the excited SPP will thereafter be damped while propagating in the material system. Another side manifestation of the 'translational-symmetry breaking' is that the orientations of dipole moments in figure 7(a), as excited by a TE-polarized light, are not pointing towards the same direction as the incidence's electric field. The directions are highly affected by the particle geometries and sometimes also affected by strong coupling by their neighbors.

5. Effect of different metal reflectors

Besides samples with a gold bottom reflector, we also made samples with silver and aluminum bottom reflectors with exactly the same preparation procedures. After these samples were annealed at 350 °C for approximately an hour, SEM images show that Au, Ag and Al samples have almost indistinguishable top-layer nanoparticles. In figure 8 we compare absorption spectra of the three types of samples. The measurements are done using an integrating sphere, which counts both specular and diffusive reflections. It is seen that the Au sample exhibits the strongest absorptivity through the visible wavelength range. The Ag and Al samples exhibit a similar level of absorptivity, especially at the center part of the spectrum. The Al sample has a slightly higher absorption in the near-UV and infrared sides of the spectrum than the Ag sample. The interband transition of silver, which occurs at a photon energy corresponding to $\lambda_0 = 300$ nm, makes the Ag sample a better absorber at the middle-UV spectrum. It is interesting to note that the maximum absorbances of the three samples, which occur around $\lambda_0 = 580$ nm, are approximately on the same level. This observation motivates that absorption of the samples around 580 nm should be mostly due to the dipole-based resonances occurring in the top-layer nanoparticles, since three samples share virtually the same top layer (as well as the spacer layer). Differences in absorptivities at shorter and larger wavelength regions should be, to a large extent, related to the substrates used. Gold, for example, exhibits high losses due to interband transitions at the short-visible wavelength range; also aluminum experiences a lossy resonance at $\lambda_0 = 820$ nm. It is however not clearly comprehensible regarding the high absorptivity of the Au sample at the long wavelength regime, since over that spectral region gold tends to be the best mirror. Collective contributions from the gold substrate and gold nanoparticles must be considered to explain its high absorptivity at NIR wavelengths.

After annealing at 500 °C, the Au and Ag samples suffer from cracks in the spacer layer (alumina) as shown in their SEM images. The non-flatness of the samples can be observed visually. Cracking of the alumina layer is potentially caused by softening and breaking of the Au and Ag reflector layers. Comparatively, the Al sample exhibits the most tolerance to high annealing temperatures; it survives well after annealing at 500 °C, as shown by figures 2(d) and (e). To complement figure 4, we show the effect of annealing temperature on the absorption spectrum of the Al sample in figure 9. Again, the measurements were done with an integrating sphere. It is clearly seen that when the annealing temperature increases, the main absorption peak becomes narrower in bandwidth and the maximum absorption strength increases. The narrowing in bandwidth can be attributed to several factors: the nanoparticles become more spherical in shape, leading to similar resonant wavelengths for surface-parallel and surface-perpendicular dipole resonances; distances between particles become larger such that resonances due to dipole–dipole interactions are less common; at the same

time the statistical size distribution of the nanoparticles has a smaller mean deviation (see supplementary data, available at stacks.iop.org/JOpt/16/025002/mmedia).

6. Conclusion

In conclusion, we have experimentally fabricated a type of three-layer plasmonic nanostructure that can efficiently absorb visible light. The preparation procedure of the samples is simple, involving just a deposition and a heat treatment. Gold nanoparticles with sizes mostly less than 50 nm are formed owing to the self-coalescence process of an ultrathin gold film. Since no lithography is used in the process, the samples can be made of large sizes. With the assistance of numerical simulations, we explained the physical mechanisms underlying their absorptive capabilities. It is found that the dipole and dipole-based resonances are vital for achieving the high efficiency of absorption. In addition, light can be coupled to the surface plasmon polariton guided by the reflector–spacer interface, which provides an additional channel for light dissipation. Samples made with a gold bottom reflector can achieve a visually black appearance, while the absorptions by samples made with silver or aluminum exhibit less overall absorption but they do have similar maximum absorptions. The absorbers can potentially be used for solar-energy harvesting especially in the field of thermophotovoltaics. The strong coloring effect as a result of light absorption can be deployed for creating durable images with a spatial resolution possibly beyond the diffraction limit of light. Strong electromagnetic fields at the top surface of such samples can be used to amplify nonlinear optical phenomena or light emission characteristics of quantum-dot systems, etc.

Acknowledgments

This work is supported by the Swedish Research Council (VR) and VR's Linnaeus center in Advanced Optics and Photonics (ADOPT).

References

[1] Siedentopf H and Zsigmondy R 1902 Uber sichtbarmachung und größen bestimmung ultramikoskopischer teilchen, mit besonderer anwendung auf goldrubingläser *Ann. Phys.* **315** 1–39

[2] Garnett J C M 1904 Clours in metal glasses and in metallic films *Phil. Trans. R. Soc.* A **203** 385–420

[3] Garnett J C M 1905 Colors in metal glasses, in metallic films, and in metallic solutions. ii *Phil. Trans. R. Soc.* A **205** 237–88

[4] Doremus R H 1966 Optical properties of thin metallic films in island form *J. Appl. Phys.* **37** 2775–81

[5] Kennerly S W, Little J W, Warmack R J and Ferrell T L 1984 Optical properties of heated Ag films *Phys Rev.* B B **29** 2926–9

[6] Craighead H G and Niklasson G A 1984 Characterization and optical properties of arrays of small gold particles *Appl. Phys. Lett.* **44** 1134–6

[7] Niklasson G and Craighead H 1985 Optical response and fabrication of regular arrays of ultrasmall gold particles *Thin Solid Films* **125** 165–70

[8] Royer P, Goudonnet J P, Warmack R J and Ferrell T L 1987 Substrate effects on surface-plasmon spectra in metal-island films *Phys Rev.* B B **35** 3753–9

[9] Niklasson G, Bobbert P and Craighead H 1999 Optical properties of square lattices of gold nanoparticles *Nanostruct. Mater.* **12** 725–30

[10] Kaiser N 2002 Review of the fundamentals of thin-film growth *Appl. Opt.* **41** 3053–60

[11] Ung T, Liz-Marzán L M and Mulvaney P 2002 Gold nanoparticle thin films *Colloids Surf.* A **202** 119–26

[12] Gupta G, Tanaka D, Ito Y, Shibata D, Shimojo M, Furuya K, Mitsui K and Kajikawa K 2009 Absorption spectroscopy of gold nanoisland films: optical and structural characterization *Nanotechnology* **20** 025703

[13] Kreibig U and Vollmer M 1995 *Optical Properties of Metal Clusters* (Berlin: Springer)

[14] Leitner A, Zhao Z, Brunner H, Aussenegg F R and Wokaun A 1993 Optical properties of a metal island film close to a smooth metal surface *Appl. Opt.* **32** 102–10

[15] Monard H and Sabary F 1997 Optical properties of silver, gold and aluminum ultra-thin granular films evaporated on oxidized aluminum *Thin Solid Films* **310** 265–73

[16] Nordlander P and Prodan E 2004 Plasmon hybridization in nanoparticles near metallic surfaces *Nano Lett.* **4** 2209–13

[17] Liu N, Mesch M, Weiss T, Hentschel M and Giessen H 2010 Infrared perfect absorber and its application as plasmonic sensor *Nano Lett.* **10** 2342–8

[18] Hao J, Wang J, Liu X, Padilla W J, Zhou L and Qiu M 2010 High performance optical absorber based on a plasmonic metamaterial *Appl. Phys. Lett.* **96** 251104

[19] Hägglund C, Zeltzer G, Ruiz R, Thomann I, Lee H-B-R, Brongersma M L and Bent S F 2013 Self-assembly based plasmonic arrays tuned by atomic layer deposition for extreme visible light absorption *Nano Lett.* **13** 3352–7

[20] Aydin K, Ferry V E, Briggs R M and Atwater H A 2011 Broadband polarization-independent resonant light absorption using ultrathin plasmonic super absorbers *Nature Commun.* **2** 517

[21] Nielsen M G, Pors A, Albrektsen O and Bozhevolnyi S I 2012 Efficient absorption of visible radiation by gap plasmon resonators *Opt. Express* **20** 13311–9

[22] Moreau A, Cirací, Mock J J, Hill R T, Wang Q, Wiley B J, Chilkoti A and Smith D R 2012 Controlled-reflectance surfaces with film-coupled colloidal nanoantennas *Nature* **492** 86–9

[23] Dai J, Ye F, Chen Y, Muhammed M, Qiu M and Yan M 2013 Light absorber based on nano-spheres on a substrate reflector *Opt. Express* **21** 6697–706

[24] Hedayati M K, Javaherirahim M, Mozooni B, Abdelaziz R, Tavassolizadeh A, Chakravadhanula V S K, Zaporojtchenko V, Strunkus T, Faupel F and Elbahri M 2011 Design of a perfect black absorber at visible frequencies using plasmonic metamaterials *Adv. Mater.* **23** 5410–4

[25] Fredriksson H, Alaverdyan Y, Dmitriev A, Langhammer C, Sutherland D, Zch M and Kasemo B 2007 Holemask colloidal lithography *Adv. Mater.* **19** 4297–302

[26] Janicki V, Amotchkina T V, Sancho-Parramon J, Zorc H, Trubetskov M K and Tikhonravov A V 2011 Design and production of bicolour reflecting coatings with Au metal island films *Opt. Express* **19** 25521–7

[27] Nielsen M G, Pors A, Albrektsen O and Bozhevolnyi S I 2012 Efficient absorption of visible radiation by gap plasmon resonators *Opt. Express* **20** 13311–9

[28] Bozhevolnyi S I and Søndergaard T 2007 General properties of slow-plasmon resonant nanostructures: nano-antennas and resonators *Opt. Express* **15** 10869–77
[29] Yan M 2013 Metal–insulator–metal light absorber: a continuous structure *J. Opt.* **15** 025006
[30] Johnson P B and Christy R W 1972 Optical constants of the noble metals *Phys Rev.* B B **6** 4370–9
[31] Palik E D 1985 *Handbook of Optical Constants of Solids* (New York: Academic)
[32] Chettiar U, Nyga P, Thoreson M, Kildishev A, Drachev V and Shalaev V 2010 FDTD modeling of realistic semicontinuous metal films *Appl. Phys.* B **100** 159–68
[33] Hao E and Schatz G C 2004 Electromagnetic fields around silver nanoparticles and dimers *J. Chem. Phys.* **120** 357–66
[34] Satoh N, Hasegawa H, Tsujii K and Kimura K 1994 Photoinduced coagulation of Au nanocolloids *J. Phys. Chem.* **98** 2143–7